ADVANCED MATERIALS
www.advmat.de

Structural Insight in the Interfacial Effect in Ferroelectric Polymer Nanocomposites

*Yang Liu, Tiannan Yang, Bing Zhang, Teague Williams, Yen-Ting Lin, Li Li, Yao Zhou, Wenchang Lu, Seong H. Kim, Long-Qing Chen, J. Bernholc, and Qing Wang**

Both experimental results and theoretical models suggest the decisive role of the filler–matrix interfaces on the dielectric, piezoelectric, pyroelectric, and electrocaloric properties of ferroelectric polymer nanocomposites. However, there remains a lack of direct structural evidence to support the so-called interfacial effect in dielectric nanocomposites. Here, a chemical mapping of the interfacial coupling between the nanofiller and the polymer matrix in ferroelectric polymer nanocomposites by combining atomic force microscopy–infrared spectroscopy (AFM–IR) with first-principles calculations and phase-field simulations is provided. The addition of ceramic fillers into a ferroelectric polymer leads to augmentation of the local conformational disorder in the vicinity of the interface, resulting in the local stabilization of the all-*trans* conformation (i.e., the polar β phase). The formation of highly polar and inhomogeneous interfacial regions, which is further enhanced with a decrease of the filler size, has been identified experimentally and verified by phase-field simulations and density functional theory (DFT) calculations. This work offers unprecedented structural insights into the configurational disorder-induced interfacial effect and will enable rational design and molecular engineering of the filler–matrix interfaces of electroactive polymer nanocomposites to boost their collective properties.

Recent advances in the assembly of ceramic oxides and ferroelectric polymers to create ferroelectric polymer nanocomposites have provided a fertile new ground for controlling and enhancing the dielectric, pyroelectric, and piezoelectric properties, and the breakdown strength of ferroelectric materials.[1–6] For instance, it has been shown that the electric polarization of a nanocomposite can be tailored through a proper filler and interface design to exceed those of its ceramic and polymer components.[7] The electrocaloric responses in terms of isothermal heat, isothermal entropy change, and adiabatic temperature change of ferroelectric polymer nanocomposites were found to be far greater than the sums of the respective values of the components.[8–11] Consequently, along with the inherent advantages of their facile processability, mechanical flexibility, and light weight property, ferroelectric polymer nanocomposites have been extensively explored for applications in high-energy-density capacitors, electrocaloric refrigeration, sensors, and energy harvesting devices.[12–18] The unforeseen collective properties of ferroelectric polymer composites are often attributed to the critical role of the filler–matrix interface,[12–18] although the origin of the physical, chemical, and electrical interactions between nanofillers and polymer matrix remains mostly unknown.

A variety of models of the filler–matrix interfaces have been proposed to comprehend the experimental results for polymer nanocomposites.[19–24] For example, Lewis argued the existence of an interfacial region between the two dielectric media, which displays different properties than those of its two constituents, and dictates the dielectric properties of the nanocomposite.[19,20] Tanaka et al. proposed a multicore model which divides the interphase into three layers: the bonded layer (1 nm), the bound layer (2–9 nm), and the loose layer (10–100 nm).[21] It was assumed that the chemical bonds between the bonded layer and the filler are the strongest, which affords the so-called interfacial polarization, also known as the Maxwell–Wagner–Sillars effect. Li attributed the enhanced electric polarization of the composites to the exchange coupling effect of the interfaces.[22] The interfacial polarization has been the most sought-after concept in the field of dielectric polymer nanocomposites in order to account for their extraordinary electric polarization and dielectric properties.[12–18] However, in stark contrast to the interfaces in semiconductor and oxide heterostructures that can be readily resolved in high-resolution transmission electron

Dr. Y. Liu, Dr. T. Yang, L. Li, Dr. Y. Zhou, Prof. L.-Q. Chen, Prof. Q. Wang
Department of Materials Science and Engineering
The Pennsylvania State University
University Park, PA 16802, USA
E-mail: wang@matse.psu.edu
Dr. B. Zhang, Prof. W. Lu, Prof. J. Bernholc
Department of Physics
North Carolina State University
Raleigh, NC 27695, USA
T. Williams
Materials Research Institute
The Pennsylvania State University
University Park, PA 16802, USA
Y.-T. Lin, Prof. S. H. Kim
Department of Chemical Engineering
The Pennsylvania State University
University Park, PA 16802, USA
The ORCID identification number(s) for the author(s) of this article can be found under https://doi.org/10.1002/adma.202005431.

DOI: 10.1002/adma.202005431

microscopy,[25] experimental investigation of the filler–matrix interfaces in polymer nanocomposites has been a daunting challenge. The lack of direct observation and characterization of the filler–matrix interfaces severely hampers theoretical studies, leaving the hypothesis proposed in phenomenological models experimentally unjustified. More recently, the scanning probe microscopy techniques with nanoscale spatial resolution are emerging as powerful tools for probing interfaces in ferroelectric polymer nanocomposites.[26–30] For instance, the local electric polarization and charge distribution at the interfaces have been investigated by intermodulation electrostatic force microscopy and Kelvin probe force microscopy.[26,27,30] However, while these measurements spatially resolve the surface potential of the samples, they are unable to uncover the chemical changes across at the interfaces of the nanocomposites. Herein we use atomic force microscopy–infrared spectroscopy (AFM–IR),[31,32] in combination with phase-field simulations and first-principles calculations, to provide, for the first time, direct structural analysis of the interfaces in ferroelectric polymer composites at the molecular level.

As illustrated in **Figure 1**a, AFM–IR operates based on the photothermal effect triggered by a pulsed IR quantum cascade laser (QCL) source.[31,32] The rapid photothermal expansion of the sample due to the absorption of infrared radiation is directly measured by the AFM cantilever. In tapping AFM–IR mode, the tip is in intermittent contact with the sample. The drive frequencies corresponding to the first two eigenmodes of cantilever motion are identified and the cantilever is driven slightly off-resonance (typically 5%) from the first mode. The IR QCL is pulsed at a frequency matching the difference between the first two drive frequencies resulting in non-linear mixing. AFM–IR absorption spectra are obtained by sweeping the frequency of incident IR light using the coupled QCL within the spectral range of interest and measuring the cantilever oscillation ring-down amplitude. The oscillation ring-down amplitude is directly proportional to the absorption coefficient of the nanoscale region of the sample under the AFM probe tip. In addition, the absorption of a specific region can be recorded by tuning the laser to a fixed wavelength to provide a chemical mapping of the region. AFM–IR has been used to examine the solvent-induced polymer recrystallization on nanoparticle agglomerates in the polycarbonate-nanoparticle composites,[28] chemical heterogeneity in the carbon nanotubes fiber nanocomposites,[29] and the surfaces of polymer and composites films with a high sensitivity of <10 nm spatial resolution.[31,32]

The ferroelectric $BaTiO_3$ (BTO)/poly(vinylidene fluoride-trifluoroethylene-chlorofluoroethylene) [P(VDF-TrFE-CFE) 61.3/30.5/8.2 mol%] polymer composite embedded with 5 vol% BTO nanoparticles of 400 nm in diameter was prepared. An IR laser at 1275 cm^{-1}, corresponding to the all-*trans* conformation (the β phase) of poly(vinylidene fluoride) (PVDF) and its binary/ternary copolymers, was used to irradiate the sample. The topographic image and the simultaneously obtained chemical map of P(VDF-TrFE-CFE) terpolymer are shown in Figure 1b,c, respectively. Different from PVDF and poly(vinylidene fluoride-trifluoroethylene) P(VDF-TrFE) that are normal ferroelectric, P(VDF-TrFE-CFE) is a relaxor ferroelectric without long-range ferroelectric order.[33–36] Accordingly, the all-*trans* conformation in the relaxor terpolymer is disordered, which is directly imaged in Figure 1c showing a dramatic spatial variation in the chemical pattern. A control measurement was performed at 1400 cm^{-1}, displaying a nearly homogeneous pattern (Figure 1d). Moreover, the chemical mappings at 1275 and 1400 cm^{-1} both present no obvious correlation with the AFM topography. These results rule out the contribution of surface topographic artifacts to the striking contrast shown in Figure 1c and confirm that the contrast arises from a difference in the chemical composition. In addition, Figure 1c suggests that the typical size of conformational disorder regions in the relaxor polymer is around

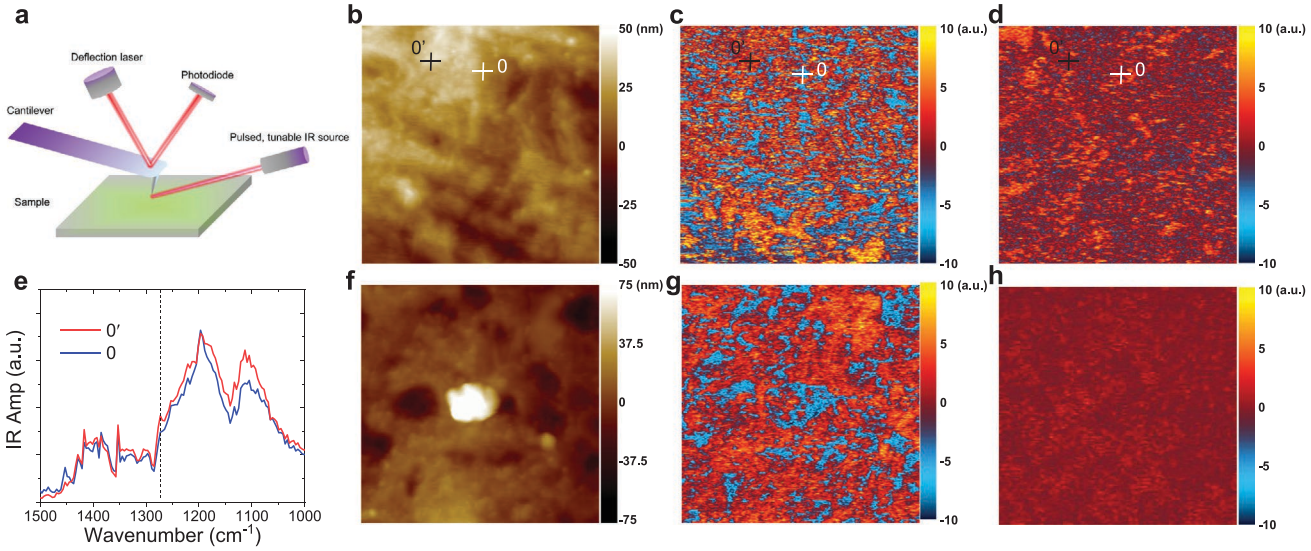

Figure 1. a) Schematic of AFM–IR setup. b) Simultaneously measured topography (2 × 2 μm^2) and c,d) AFM–IR chemical maps with irradiation by a laser at 1275 cm^{-1} and 1400 cm^{-1}, respectively, of P(VDF-TrFE-CFE) terpolymer. e) Local spectra of the sites marked in (b–d). f) Simultaneously measured topography (2 × 2 μm^2) and g,h) AFM–IR chemical maps with irradiation by a laser at 1275 and 1400 cm^{-1}, respectively, in the BTO/P(VDF-TrFE-CFE) nanocomposites with BTO of 400 nm in diameter.

tens to hundreds of nanometers, which is larger than the counterpart of the so-called polar nanoregions (typically several to tens of nanometers) in perovskite relaxors.[37–40] The local conformational disorder in the relaxor terpolymer is also validated by a strong local IR change at 1275 cm^{-1} according to the local spectra (Figure 1e).[36]

The introduction of BTO fillers into the polymer (Figure 1f) significantly alters the local 1275 cm^{-1} band of the all-*trans* conformation (Figure 1g). Specifically, the size of conformational disorder (red region) in the composite is appreciably enlarged, which is a reflection of the fact that the all-*trans* conformation is locally stabilized in the polymer composite. Comparatively, no significant changes were observed in the chemical map at 1400 cm^{-1} of the composite (Figure 1h) relative to that of the terpolymer, which reaffirms that the conformational disorder originates from the chemical composition rather than surface artifacts.

As shown in **Figure 2**a,d, AFM–IR measurements were carried out on the randomly selected areas of the composite. The IR amplitude at 1275 cm^{-1} of the composite was normalized by the reference IR value of P(VDF-TrFE-CFE) (site 0 in Figure 1e). It is worth mentioning the interface-induced modification of IR response (e.g., sites 2 and 3) is greater than the maximum fluctuation in the IR amplitude caused by the conformational disorder in the relaxor polymer (Figure 2b,c). It is found that while sites 2 and 3, which are ≈40 and ≈15 nm, respectively, away from the interface, exhibit the increment of the all-*trans* conformation, the magnitude of 1275 cm^{-1} band at site 1, which is ≈1 nm away from the interface, is reduced. The absence of the IR peak appearing at 1275 cm^{-1} at site 4 (≈50 nm away from the interface) denotes the absence of the interfacial coupling effect. The spatial AFM–IR results contradict the multi-core model, in which the interfacial effect is hypothesized to be a function of the distance away from the boundary between the polymer and the filler, giving rise to the strongest chemical interactions at the closest position to the interface. Concomitantly, the AFM–IR results clearly manifest the inhomogeneous nature of the interfacial coupling, which is not present in the multicore model and other models.[19–23] The highly inhomogeneous feature of the interfacial coupling is further attested when the measured positions were moved to >100 nm away from the filler–matrix interface. The all-*trans* conformation at 1275 cm^{-1} is enhanced at sites 6 and 7 (Figure 2e,f) and substantially reduced at site 5. The strongest enhancement occurs at site 7, which is ≈150 nm away from the interface. This is also an unexpected result, according to the multicore model.[21] As the Gouy–Chapman diffuse layer with the Debye shielding length is speculated to be in a range of several tens to a hundred nanometers, the electric double layer superimposed on the interfacial layer should vanish at locations that are >100 nm away from the interface,[19,20] resulting in a bulk-like conformation and yielding negligible interfacial effect. The existence of a considerable discrepancy between our experimental observations and the model is also confirmed in our measurements of additional positions that are ≈100 nm away from the interface as shown in Figure S1, Supporting Information.

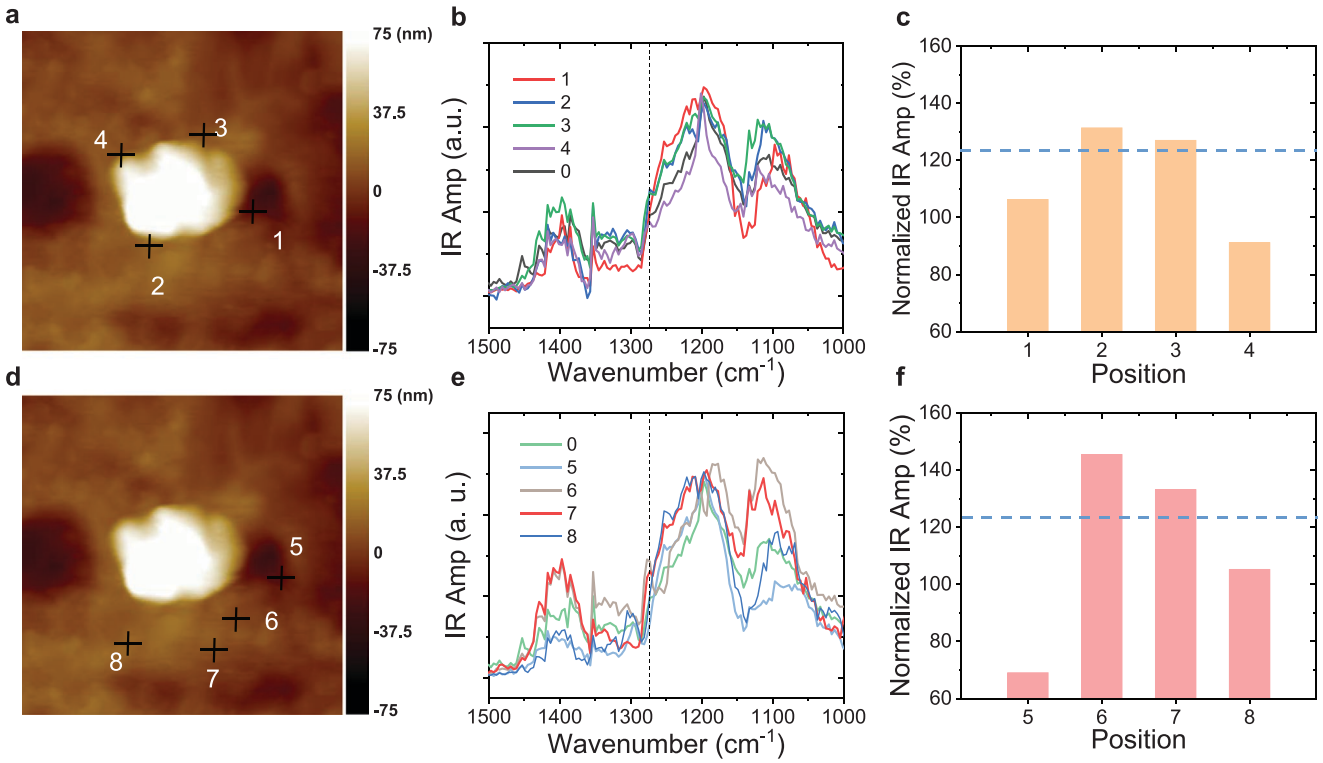

Figure 2. a) The topography (1 × 1 μm²) and positions 1–4. b) Local IR spectra at different sites as marked in (a). c) Normalized IR response at 1275 cm^{-1}. The dashed line corresponds to the IR fluctuation caused by conformational disorder in the relaxor terpolymer. d) AFM topography (1 × 1 μm²) and positions 5–8. e) Local IR spectra at different sites as marked in (d). f) Normalized IR response at 1275 cm^{-1}. The dashed line corresponds to the IR fluctuation caused by conformational disorder in the relaxor terpolymer.

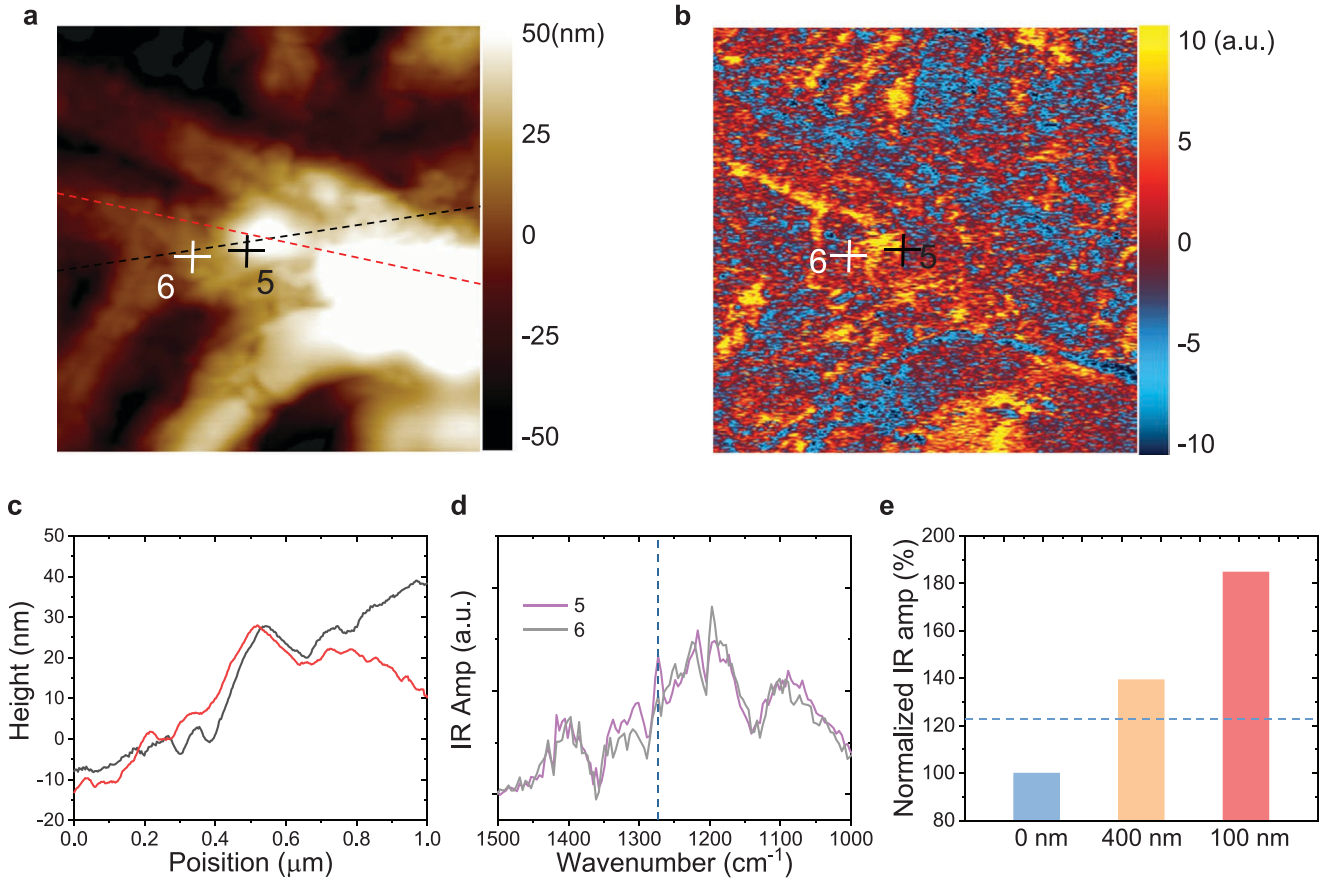

Figure 3. a) AFM–IR topography ($1 \times 1\ \mu m^2$), b) chemical map irradiated with 1275 cm^{-1}, c) AFM height profile versus position, and d) local IR spectra in BTO/P(VDF-TrFE-CFE) with BTO of 100 nm in diameter. The dashed line indicates the IR band characteristic of the all-*trans* conformation. e) Comparison of the local IR response between terpolymer and the composites with different filler sizes where the IR amplitude at site 3 at 1275 cm^{-1} is set as a reference.

We next investigate the effect of the filler size on the interfacial polarization in the composites. There is a controversy regarding the dependence of the dielectric constants of the composites on the filler size as both decreases and increases of the dielectric constants have been reported in ferroelectric polymer composites, such as BTO/PVDF and BTO/P(VDF-TrFE), as the filler size is decreased.[24,41–45] On the other hand, the most recent investigation of interfacial polarization using Kelvin probe force microscopy shows nearly no size dependence.[27] **Figure 3** shows the AFM–IR results on the terpolymer composite incorporated with BTO of 100 nm in diameter. The bright region with a larger height shown in the AFM topography (Figure 3a) is attributed to polymer chain overlaps, in addition to a particle at the center, which is verified by the AFM height profile (Figure 3c). Remarkably, while the addition of the 100-nm BTO particles enhances greatly the conformational disorder, in accord with the above results for the composite with 400-nm BTO, the conformational disorder becomes more pronounced in the composite with 100-nm BTO according to the local IR spectra near the interface as compared in Figure 3d,e. This result demonstrates the existence of the size-driven enhancement of the local all-*trans* chain conformation in the composites, which provides an explanation for the improvements in the electric polarization and the dielectric constants of the polymer composites with small-sized fillers reported in the majority of the literature.[12–18]

Phase-field simulations were performed to verify the AFM–IR results. As shown in **Figure 4**a,b, our simulations reveal an enhanced polarization around the interfacial regions, in agreement with the experimental results, and substantiate a higher polarization of the composite with 100 nm of BTO, that is, the average polarizations are 0.063 and 0.068 C m^{-2} for the composites with 400- and 100-nm BTO, respectively. Moreover, the theoretical results conclude that the spatial inhomogeneity of the polarization around the interfacial regions is mostly caused by the electrostatic interaction within the composite where an inhomogeneous depolarization field generated by the multidomain structure locally enhances or suppresses the polarization. To further support this scenario, we performed phase-field simulations on the composite without the electrostatic interaction. As shown in Figure 4c after the electrostatic interaction is eliminated, the polarization magnitude around the interface region becomes more spatially homogeneous with respect to the actual case shown in Figure 4a.

To gain deeper insights into the interface, we analyze the BTO/P(VDF-TrFE-CFE) interface by using density functional theory (DFT). The relaxed interface structure and the calculated dipole moment are summarized in Figure 4d. Since the relaxor

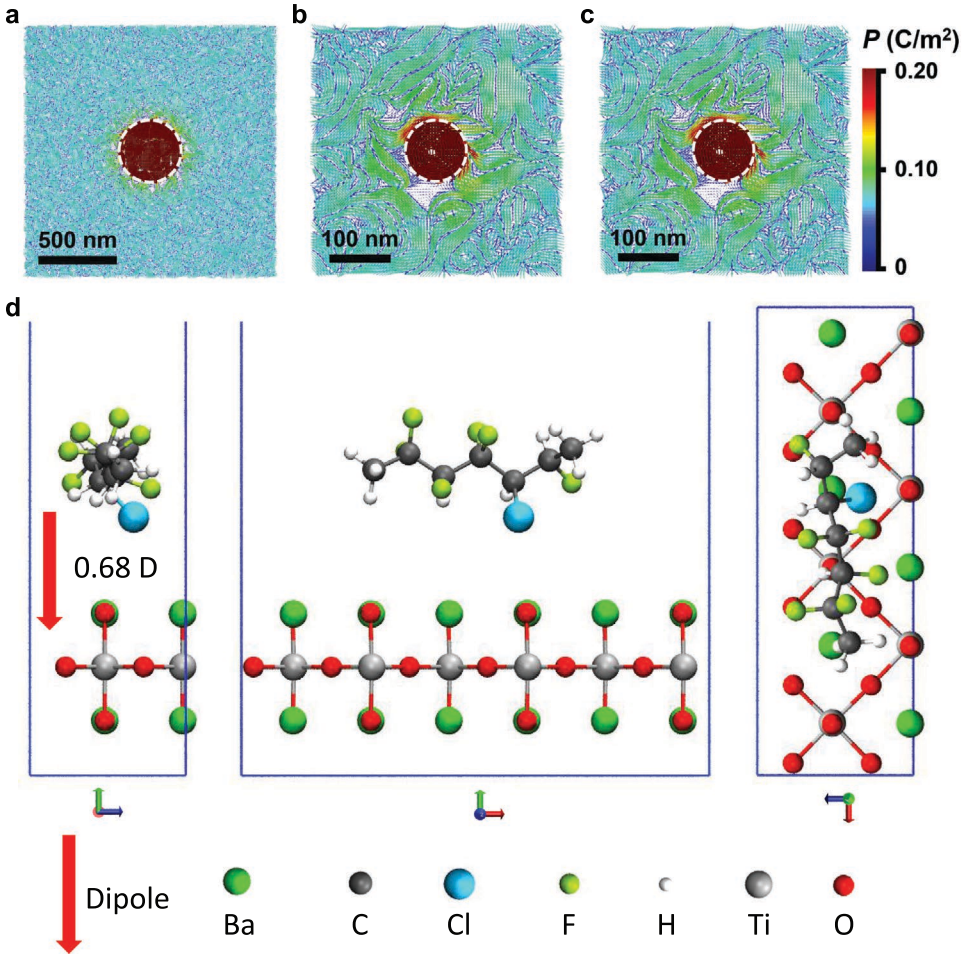

Figure 4. a,b) Mapping of the polarization field around a BTO particle in the BTO/P(VDF-TrFE-CFE) composites with particle diameters of 400 nm (a) and 100 nm (b), respectively, from phase-field simulations. c) Mapping of the polarization field around a BTO particle in the BTO/P(VDF-TrFE-CFE) composite with particle diameters of 400 nm, from phase-field simulations after eliminating the electrostatic interaction. The polarization field is represented by the arrow glyphs, where the color of the arrows indicates the polarization magnitude, as shown by the color bar. The white dashed circle indicates a BTO particle. d) The relaxed interface structure in BTO/P(VDF-TrFE-CFE) composites obtained by density functional theory. The geometry is shown along three orthogonal views: perpendicular and parallel to the chain direction, and on top. The dipole moment is 0.68 D and the red arrow indicates its direction.

polymer is macroscopically paraelectric without spontaneous electric polarization, the DFT simulations suggest that, as a result of reorientation of the relaxed P(VDF-TrFE-CFE) chain at the interface in the composite, there exists a dipole moment of 0.68 D, perpendicular to both the BTO surface and the P(VDF-TrFE-CFE) chain. This DFT result uncovers the microscopic origin of the enhanced polar conformation observed in the AFM–IR results and the improved polarization predicted by the phase-field simulations.

We also study the effect of surface-modified fillers on the interfacial coupling using the PVDF/BTO nanocomposites. The AFM–IR results of the composites are summarized and compared in **Figure 5** and Figure S2, Supporting Information. The PVDF nanocomposite with pristine BTO shows an inhomogeneous chemical pattern (Figure 5b) and distance-dependent interfacial coupling behavior (Figure 5c,g), which are similar to those found in P(VDF-TrFE-CFE)/BTO nanocomposites (Figures 1 and 2). Although the introduction of surface-modified fillers leads to an increase in the uniformity of chemical pattern (Figure 5e), the chemical pattern near interface region remains inhomogeneous (Figure 5e). While the local spectra of the composite with surface-functionalized fillers show a position-dependent distribution (Figure 5f,h), the variation between different local positions is smaller than that of the composite embedded with pristine fillers (Figure 5g). Moreover, we find that the position 3 and position 7 exhibit a reduced IR response at 837 cm^{-1}, which is another key characteristic IR band of all-*trans* conformation in PVDF. This result is indicative of a local decrease in the polar configuration close to the interface, which again proves that the multicore model cannot explain the experimental results. Note that, in addition to the conformational disorders, chain mobility, crystallinity, and degree of the stoichiometry may also play important roles in determining the local properties of the interface region.[21,27,46]

In summary, by combining nanoscale IR imaging with phase-field calculations and atomic-scale simulations, we have provided a spatial structure analysis of the filler–matrix interfaces in ferroelectric polymer nanocomposites. Amplified

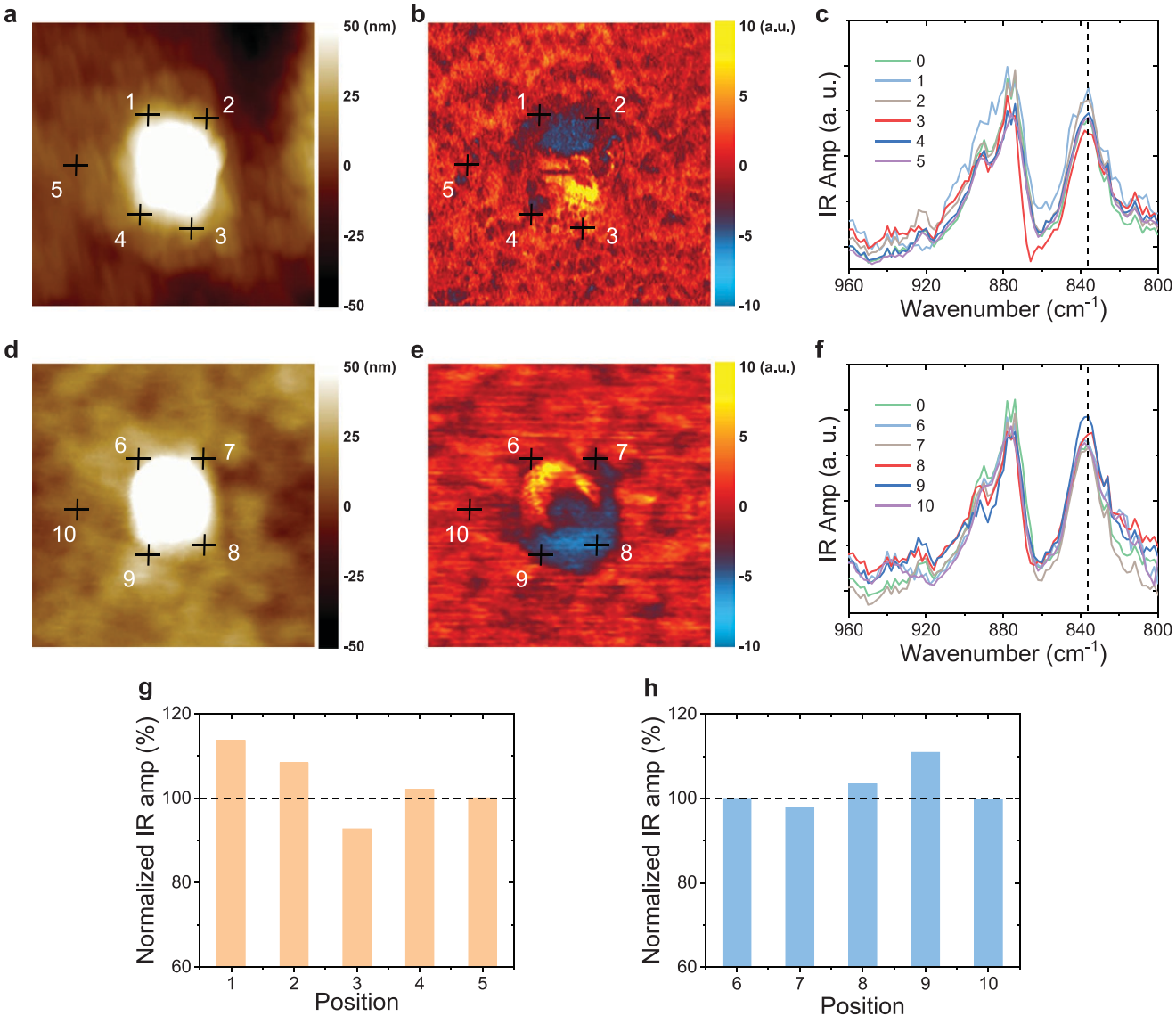

Figure 5. a) AFM–IR topography (1 × 1 μm^2), b) chemical map with irradiation at 837 cm^{-1}, and c) local IR spectra in BTO/PVDF without surface modifications. d) AFM–IR topography (1 × 1 μm^2), e) chemical map with irradiation at 837 cm^{-1}, and f) local IR spectra in BTO/PVDF with surface modifications. The result from neat PVDF is indexed as 0 in (e) and (f). The dashed lines are a guide for the wavenumber of 837 cm^{-1}. g) Normalized IR response at 837 cm^{-1} without surface modifications. h) Normalized IR response at 837 cm^{-1} with surface modifications.

conformational disorder, which is consistent with the findings in non-ferroelectric polymer based composites,[47,48] and interface-induced stabilization of the all-*trans* chain conformation have been uncovered in the nanocomposites, which are further enhanced with a reduced filler size. Meanwhile, we show the highly inhomogeneous nature of the interfacial coupling in both the composites with pristine and surface-functionalized fillers, with the largest interfacial coupling occurring far beyond the bonded layer predicted by the well-established multicore model. The formation of polar interface regions, confirmed by DFT calculations, unambiguously demonstrates the dominant contribution of the interfacial effect to the electric polarization of the composites from the structural point of view. This work provides direct structural evidence supporting the critical role of the interfacial coupling effect reported in high-performance electrocaloric, capacitive, piezoelectric, and pyroelectric polymer nanocomposites. Moreover, the insights into the interfacial coupling at the molecular level open up prospects for developing new interfacial strategies to realize improved properties and unlock new functionalities in ferroelectric polymer nanocomposites.

Experimental Section

Sample Preparation: BTO nanoparticles were purchased from US-Nano (99.9%, 400 nm, tetragonal; 99.9%, 100 nm, cubic). P(VDF-TrFE-CFE) was synthesized via suspension polymerization.[49] P(VDF-TrFE-CFE) powders were dissolved in *N*,*N*-dimethylformamide (DMF, Sigma-Aldrich, ACS, 99.8%), and stirred overnight to give a homogeneous solution at a concentration of 40 mg ml^{-1}. BTO

nanoparticles were mixed with P(VDF-TrFE-CFE) solution in a ratio of 5 vol%. After stirring overnight, the dispersion was subjected to a 15-min tip-type sonication (175 W, 500 W × 35%) before drop-casting on glass plates. The cast films were first dried at 75 °C for 12 h in a vacuum oven to completely remove the solvent, followed by annealing at 105 °C for 12 h, then cooled down to room temperature. The typical thickness of the nanocomposite films is 15 µm.

The surface modification of BTO nanoparticles was conducted as schemed in Figure S3, Supporting Information.[50] Typically, a certain amount of BTO nanoparticles was firstly dispersed in ethanol and stirred for 1.5 h, and then ultrasonicated for 1 h to form a homogeneous suspension. (3-Aminopropyl)triethoxysilane (KH550) with a concentration of 1 wt% to BTO nanoparticles was added dropwise with continuous stirring for 12 h. After that, the mixture was centrifuged at 8000 rpm for 12 min and then washed with ethanol three times to remove excess KH550. After being dried in a vacuum oven at 60 °C for 24 h, the obtained white powers were collected.

The PVDF-based nanocomposites films were prepared using a typical solution-casting method. Typically, a certain amount of PVDF powders was dissolved in DMF and stirred for 24 h. The KH550 modified BTO nanoparticles were then added (the volume fraction was set as 5 vol%), followed by sonication for 25 min using a high-power programmable sonicator with a tip to yield a homogeneous suspension. The obtained solution was then cast onto a pre-cleaned quartz glass substrate and dried in an oven at 70 °C for 12 h. The obtained films were then peeled off and put in a vacuum oven at 120 °C for 24 h to completely remove the solvent. The thickness of the nanocomposites films was ≈10–20 µm.

Characterization: AFM–IR measurement was conducted on an Anasys nanoIR3 (Bruker) system equipped with a HYPERspectra QCL with the spectral resolution set to 4 cm^{-1}. For the terpolymer/BTO samples, both the height and chemical composition maps were simultaneously obtained using a PR-EX-TNIR-A probe in tapping AFM–IR mode. The spectra in the range of 1000–1500 cm^{-1} were recorded by placing the AFM probe with spatial resolution ≈10 nm on top of the samples. Amplitude setpoint ratios for the AFM scans varied slightly to compensate for topography; the ratio was held in the moderate tapping range (0.6–0.8) for all presented scans. Each of the IR data is an average of 10 measurements.

For the PVDF/BTO samples, AFM–IR experiment was operated using a top-down-illumination NanoIR3 system (Bruker) and gold-coated silicon nitride probes (0.07–0.4 N m^{-1} spring constant, 13 ± 4 kHz resonant frequency, Bruker). The laser source in the NanoIR3 system was a tunable QCL IR laser with a repetition rate tuned to match the contact resonance frequency of the sample-probe contact interface. AFM–IR spectra were measured 8 times with a 2 cm^{-1} resolution at each location and then averaged to improve the signal-to-noise ratio. For AFM–IR mapping, the scan rate was set to 1 Hz with 256 pixels per line scan and the phase-lock-loop (PLL) (Threshold 0.5, iGain 0.1, pGain 20) was enabled to keep the QCL repetition rate at the contact resonance frequency.

Phase-Field Model: Phase-field simulations were performed on the composites consisting of a circular BTO particle inside a P(VDF-TrFE-CFE) matrix. The composites with 400-nm and 100-nm BTO particles were simulated with the total system sizes of 1584 × 1584 and 396 × 396 nm^2, respectively. The BTO particle fraction was 5 vol% of the simulation system in both cases. The P(VDF-TrFE-CFE) matrix adopted a random crystallographic orientation with a correlation length of 80 nm.

The evolution of the polarization field was described by the time-dependent Ginzburg–Landau equation,[51]

$$\frac{\partial \mathbf{P}}{\partial t} = -L\frac{\delta F}{\delta \mathbf{P}} \tag{1}$$

where the free energy F is given by the sum of the Landau free energy, the electrostatic energy, and the gradient energy. The Landau free energy of BTO and BZT was the same as that in ref. [54]. The Landau free energy of P(VDF-TrFE-CFE) adopted the form of

$$F_{\text{Landau}} = a_1 P_1^2 + a_2\left(P_2^2 + P_3^2\right) + a_{11}P_1^4 + a_{111}P_1^6 \tag{2}$$

to describe a ferroelectric phase with a spontaneous polarization along the x_1 axis of the local crystal coordinate. The electrostatic energy and the gradient energy followed the same formulations as those in Ref. [52].

Density Functional Theory Calculations: The interface was modeled by a P(VDF-TrFE-CFE) chain on top of a BTO surface in a unit cell, shown in Figure 4d P(VDF-TrFE-CFE) chain was modeled as H–(CH_2–CF_2–CFH–CF_2–CClH–CFH)–CH_3. BTO surface was modeled by a three-layer (BaO-TiO_2-BaO) (001) slab of cubic-phase BTO.

During the simulation, a unit cell of a P(VDF-TrFE-CFE) chain was relaxed under 0 pressure. Then the relaxed P(VDF-TrFE-CFE) chain was placed on top of a BTO surface, with its axis aligned parallel to the (110) direction of BTO, serving as the interface model. During the relaxation, to stabilize the BTO structure, the bottom BO layer of BTO was fixed while the atoms in the other two layers of BTO and the P(VDF-TrFE-CFE) chain were free to move. After the structure was relaxed, a Berry's Phase calculation was performed on the relaxed P(VDF-TrFE-CFE) chain to calculate the dipole moment.[53]

The DFT and Berry's phase calculations were performed using the open-source package Quantum Espresso,[54] with Perdew–Burke–Ernzerhof exchange-correlation functional,[55] ultrasoft pseudopotentials.[56] The unit cell dimensions were 17.085 × 20.000 × 5.695 Å. The Monkhorst–Pack 1 × 1 × 4 grid was used to sample the Brillouin zone.[57] The planewave kinetic energy cutoffs were 60 Rydbergs for the wave functions and 600 Rydbergs for the charge density. The convergence thresholds were 0.0001 Rydberg for the total energy, 0.001 Rydberg/a_0 ($1a_0$ = 0.529 Å) for the Cartesian components of the forces, and 0.3 kilobar for pressure.

Supporting Information

Supporting Information is available from the Wiley Online Library or from the author.

Acknowledgements

This research was funded by the US Air Force Office of Scientific Research (FA9550-19-1-0008, Q.W.) and the US Office of Naval Research (N000141912033, J.B.). The phase-field simulation effort is partially supported by NSF under DMR-1744213. The supercomputer time was provided at the Oak Ridge Leadership Computing Facility at ORNL, supported by DOE contract DE-AC05-00OR22725 (J.B.). The authors would like to thank the Penn State Materials Characterization Lab and Bruker Nano for the use of the equipment and instrument expertise.

Conflict of Interest

The authors declare no conflict of interest.

Keywords

atomic force microscopy–infrared spectroscopy, ferroelectrics, filler–matrix interfaces, interfacial effects, polymer nanocomposites

Received: August 11, 2020
Revised: September 29, 2020
Published online: November 4, 2020

[1] P. Barber, S. Balasubramanian, Y. Anguchamy, S. Gong, A. Wibowo, H. S. Gao, H. J. Ploehn, H.-C. zur Loye, *Materials* **2009**, *2*, 1697.
[2] H. Li, F. Liu, B. Fan, D. Ai, Z. Peng, Q. Wang, *Small Methods* **2018**, *2*, 1700399.

[3] C. J. Dias, D. K. Das-Gupta, *IEEE Trans. Dielectr. Electr. Insul.* **1996**, *3*, 706.
[4] A. K. Batra, M. D. Aggarwal, M. E. Edwards, A. Bhalla, *Ferroelectrics* **2008**, *366*, 84.
[5] K. S. Ramadan, D. Sameoto, S. Evoy, *Smart Mater. Struct.* **2014**, *23*, 033001.
[6] W. A. D. M. Jayathilaka, K. Qi, Y. Qin, A. Chinnappan, W. Serrano, C. Baskar, H. Wang, J. He, S. Cui, S. W. Thomas, S. Ramakrishna, *Adv. Mater.* **2019**, *31*, 1805921.
[7] T. Zhang, X. Chen, Y. Thakur, B. Lu, Q. Y. Zhang, J. Runt, Q. M. Zhang, *Sci. Adv.* **2020**, *6*, eaax6622.
[8] G. Zhang, Q. Li, H. Gu, S. Jiang, K. Han, M. R. Gadinski, M. A. Haque, Q. Zhang, Q. Wang, *Adv. Mater.* **2015**, *27*, 1450.
[9] Q. Li, G. Zhang, X. Zhang, S. Jiang, Y. Zeng, Q. Wang, *Adv. Mater.* **2015**, *27*, 2236.
[10] J. Qian, R. Peng, Z. Shen, J. Jiang, F. Xue, T. N. Yang, L. Q. Chen, Y. Shen, *Adv. Mater.* **2019**, *31*, 1801949.
[11] Y. Q. Chen, J. F. Qian, J. Y. Yu, M. F. Guo, Q. H. Zhang, J. Y. Jiang, Z. H. Shen, L.-Q. Chen, Y. Shen, *Adv. Mater.* **2020**, *32*, 1907927.
[12] Q. Wang, L. Zhu, *J. Polym. Sci.,Part B: Polym. Phys.* **2011**, *49*, 1421.
[13] Z. M. Dang, J. K. Yuan, S. H. Yao, R. J. Liao, *Adv. Mater.* **2013**, *25*, 6334.
[14] X. Huang, P. Jiang, *Adv. Mater.* **2015**, *27*, 546.
[15] V. K. Thakur, R. K. Gupta, *Chem. Rev.* **2016**, *116*, 4260.
[16] Z. Pan, L. Yao, J. Zhai, X. Yao, H. Chen, *Adv. Mater.* **2018**, *30*, 1705662.
[17] Q. Li, F. Z. Yao, Y. Liu, G. Z. Zhang, H. Wang, Q. Wang, *Annu. Rev. Mater. Res.* **2018**, *48*, 219.
[18] X. Zhang, B. W. Li, L. Dong, H. X. Liu, W. Chen, Y. Shen, C. W. Nan, *Adv. Mater. Interfaces* **2018**, *5*, 1800096.
[19] T. J. Lewis, *IEEE Trans. Dielectr. Electr. Insul.* **2004**, *11*, 739.
[20] J. Lewis, *J. Phys. D: Appl. Phys.* **2005**, *38*, 202.
[21] T. Tanaka, M. Kozako, N. Fuse, Y. Ohki, *IEEE Trans. Dielectr. Electr. Insul.* **2005**, *12*, 669.
[22] J. Li, *Phys. Rev. Lett.* **2003**, *90*, 217601.
[23] L. Yu, V. Ranjan, M. B. Nardelli, J. Bernholc, *Phys. Rev. B* **2009**, *80*, 165432.
[24] S. F. Mendes, C. M. Costa, C. Caparrós, V. Sencadas, S. Lanceros-Méndez, *J. Mater. Sci.* **2012**, *47*, 1378.
[25] H. Y. Hwang, Y. Iwasa, M. Kawasaki, B. Keimer, N. Nagaosa, Y. Tokura, *Nat. Mater.* **2012**, *11*, 103.
[26] R. Borgani, L. K. H. Pallon, M. S. Hedenqvist, U. W. Gedde, D. B. Haviland, *Nano Lett.* **2016**, *16*, 5934.
[27] S. Peng, X. Yang, Y. Yang, S. Wang, Y. Zhou, J. Hu, Q. Li, J. He, *Adv. Mater.* **2019**, *31*, 1807722.
[28] P. S. Brown, B. Bhushan, *Sci. Rep.* **2016**, *6*, 21048.
[29] A. Mikhalchan, A. M. Banas, K. Banas, A. M. Borkowska, M. Nowakowski, M. B. H. Breese, W. M. Kwiatek, C. Paluszkiewicz, T. E. Tay, *Chem. Mater.* **2018**, *30*, 1856.
[30] Y.-X. Chen, X. Chen, X.-F. Zhang, Q.-D. Shen, *ACS Appl. Energy Mater.* **2020**, *3*, 3665.
[31] W. Melitz, J. Shen, A. C. Kummel, S. Lee, *Surf. Sci. Rep.* **2011**, *66*, 1.
[32] A. Dazzi, C. B. Prater, *Chem. Rev.* **2017**, *117*, 5146.
[33] Y. Liu, A. Haibibu, B. Zhang, W. H. Xu, W. C. Lu, J. Bernholc, Q. Wang, *Nature* **2018**, *562*, 96.
[34] I. Terzic, N. L. Meereboer, M. Acuautla, G. Portale, K. Loos, *Nat. Commun.* **2019**, *10*, 601.
[35] L. Yang, X. Li, E. Allahyarov, P. L. Taylor, Q. M. Zhang, L. Zhu, *Polymer* **2013**, *54*, 1709.
[36] Y. Liu, B. Zhang, W. Xu, A. Haibibu, Z. Han, W. Lu, J. Bernholc, Q. Wang, *Nat. Mater.* **2020**, *19*, 1169.
[37] G. Burns, F. H. Dacol, *Phys. Rev. B* **1983**, *28*, 2527.
[38] D. A. Tenne, A. Soukiassian, M. H. Zhu, A. M. Clark, X. X. Xi, H. Choosuwan, Q. He, R. Guo, A. S. Bhalla, *Phys. Rev. B* **2003**, *67*, 012302.
[39] M. E. Manley, J. W. Lynn, D. L. Abernathy, E. D. Specht, O. Delaire, A. R. Bishop, R. Sahul, J. D. Budai, *Nat. Commun.* **2014**, *5*, 3683.
[40] M. J. Krogstad, P. M. Gehring, S. Rosenkranz, R. Osborn, F. Ye, Y. Liu, J. P. C. Ruff, W. Chen, J. M. Wozniak, H. Luo, O. Chmaissem, Z.-G. Ye, D. Phelan, *Nat. Mater.* **2018**, *17*, 718.
[41] Z. M. Dang, H. P. Xu, H. Y. Wang, *Appl. Phys. Lett.* **2007**, *90*, 012901.
[42] M. H. Bi, Y. N. Hao, J. M. Zhang, M. Lei, K. Bi, *Nanoscale* **2017**, *9*, 16386.
[43] S. Wada, H. Yasuno, T. Hoshina, S.-M. Nam, H. Kakemoto, T. Tsurumi, *Jpn. J. Appl. Phys.* **2003**, *42*, 6188.
[44] S. Wada, A. Yazawa, T. Hoshina, Y. Kameshima, H. Kakemoto, T. Tsurumi, Y. Kuroiwa, *IEEE Trans. Ultrason. Ferroelectr. Freq. Control* **2008**, *55*, 1895.
[45] Y. P. Mao, S. Y. Mao, Z.-G. Ye, Z. X. Xie, L. S. Zheng, *J. Appl. Phys.* **2010**, *108*, 014102.
[46] S. M. Peng, Q. B. Zeng, X. Yang, J. Hu, X. H. Qiu, J. L. He, *Sci. Rep.* **2016**, *6*, 38978.
[47] P. de Gennes, *Macromolecules* **1980**, *13*, 1069.
[48] M. Müller, *Polymers at Interfaces and Surfaces and in Confined Geometries* (Eds: K. Matyjaszewski, M. Muller), Elsevier, Amsterdam **2012**.
[49] Q. Li, G. Z. Zhang, F. H. Liu, K. Han, M. R. Gadinski, C. X. Xiong, Q. Wang, *Energy Environ. Sci.* **2015**, *8*, 922.
[50] Y. Zhou, Q. Wang, *J. Appl. Phys.* **2020**, *127*, 240902.
[51] Y. Li, L. E. Cross, L.-Q. Chen, *J. Appl. Phys.* **2005**, *98*, 064101.
[52] Y. Li, S. Hu, Z.-K. Liu, L.-Q. Chen, *Acta Mater.* **2002**, *50*, 395.
[53] F. Bernardini, V. Fiorentini, D. Vanderbilt, *Phys. Rev. B* **1997**, *56*, R10024(R).
[54] P. Giannozzi, S. Baroni, N. Bonini, M. Calandra, R. Car, C. Cavazzoni, D. Ceresoli, G. L. Chiarotti, M. Cococcioni, I. Dabo, A. Dal Corso, S. de Gironcoli, S. Fabris, G. Fratesi, R. Gebauer, U. Gerstmann, C. Gougoussis, A. Kokalj, M. Lazzeri, L. Martin-Samos, N. Marzari, F. Mauri, R. Mazzarello, S. Paolini, A. Pasquarello, L. Paulatto, C. Sbraccia, S. Scandolo, G. Sclauzero, A. P. Seitsonen, A. Smogunov, P. Umari, R. M. Wentzcovitch, *J. Phys.: Condens. Matter* **2009**, *21*, 395502.
[55] J. P. Perdew, K. Burke, M. Ernzerhof, *Phys. Rev. Lett.* **1996**, *77*, 3865.
[56] D. Vanderbilt, *Phys. Rev. B* **1990**, *41*, 7892.
[57] H. J. Monkhorst, J. D. Pack, *Phys. Rev. B* **1976**, *13*, 5188.